

## Examining the impact of overlying aerosols on the retrieval of cloud optical properties from passive remote sensing

O. M. Coddington,<sup>1</sup> P. Pilewskie,<sup>1,2</sup> J. Redemann,<sup>3,4</sup> S. Platnick,<sup>5</sup> P. B. Russell,<sup>3</sup>  
K. S. Schmidt,<sup>1</sup> W. J. Gore,<sup>3</sup> J. Livingston,<sup>6</sup> G. Wind,<sup>5</sup> and T. Vukicevic<sup>7</sup>

Received 15 July 2009; revised 24 November 2009; accepted 4 January 2010; published 28 May 2010.

[1] Haywood et al. (2004) show that an aerosol layer above a cloud can cause a bias in the retrieved cloud optical thickness and effective radius. Monitoring for this potential bias is difficult because space-based passive remote sensing cannot unambiguously detect or characterize aerosol above cloud. We show that cloud retrievals from aircraft measurements above cloud and below an overlying aerosol layer are a means to test this bias. The data were collected during the Intercontinental Chemical Transport Experiment (INTEX-A) study based out of Portsmouth, New Hampshire, United States, above extensive, marine stratus cloud banks affected by industrial outflow. Solar Spectral Flux Radiometer (SSFR) irradiance measurements taken along a lower level flight leg above cloud and below aerosol were unaffected by the overlying aerosol. Along upper level flight legs, the irradiance reflected from cloud top was transmitted through an aerosol layer. We compare SSFR cloud retrievals from below-aerosol legs to satellite retrievals from the Moderate Resolution Imaging Spectroradiometer (MODIS) in order to detect an aerosol-induced bias. In regions of small variation in cloud properties, we find that SSFR and MODIS-retrieved cloud optical thickness compares within the uncertainty range for each instrument while SSFR effective radius tend to be smaller than MODIS values (by 1–2  $\mu\text{m}$ ) and at the low end of MODIS uncertainty estimates. In regions of large variation in cloud properties, differences in SSFR and MODIS-retrieved cloud optical thickness and effective radius can reach values of 10 and 10  $\mu\text{m}$ , respectively. We include aerosols in forward modeling to test the sensitivity of SSFR cloud retrievals to overlying aerosol layers. We find an overlying absorbing aerosol layer biases SSFR cloud retrievals to smaller effective radii and optical thickness while nonabsorbing aerosols had no impact.

**Citation:** Coddington, O. M., P. Pilewskie, J. Redemann, S. Platnick, P. B. Russell, K. S. Schmidt, W. J. Gore, J. Livingston, G. Wind, and T. Vukicevic (2010), Examining the impact of overlying aerosols on the retrieval of cloud optical properties from passive remote sensing, *J. Geophys. Res.*, 115, D10211, doi:10.1029/2009JD012829.

### 1. Introduction

[2] The radiative indirect aerosol effect, (also known as the first indirect aerosol effect, the cloud albedo effect, or the Twomey effect), refers to the brightening of clouds due

to aerosol effects on cloud microphysics [Twomey, 1974, 1991]. Aerosols provide an increased concentration of cloud condensation nuclei, resulting in a larger number of cloud drops. For fixed liquid water content, the increased numbers of cloud drops have smaller effective radii but present a larger net cross-sectional area, hence increasing cloud albedo. Experimental validation of the indirect aerosol effect have been made in ship tracks [Platnick et al., 2000; Coakley and Walsh, 2002] and other polluted environments [e.g., Peng et al., 2002]. Wilcox et al. [2006] determined experimentally that the indirect aerosol effect enhanced the top-of-atmosphere cooling due to shortwave cloud radiative forcing by  $-9.9 \pm 4.3 \text{ W m}^{-2}$ . However, global climate model attempts at modeling this effect have large uncertainties.

[3] A global assessment of the first indirect effect must rely on satellite observations of cloud radiative properties. Determining the impact of aerosol particles on cloud radi-

<sup>1</sup>Laboratory for Atmospheric and Space Physics, University of Colorado at Boulder, Boulder, Colorado, USA.

<sup>2</sup>Department of Atmospheric and Oceanic Sciences, University of Colorado at Boulder, Boulder, Colorado, USA.

<sup>3</sup>NASA Ames Research Center, Moffett Field, California, USA.

<sup>4</sup>Bay Area Environmental Research Institute, Sonoma, California, USA.

<sup>5</sup>NASA Goddard Space Flight Center, Greenbelt, Maryland, USA.

<sup>6</sup>Southwest Research Institute, Menlo Park, California, USA.

<sup>7</sup>NOAA Atlantic Oceanographic and Meteorological Laboratory, Miami, Florida, USA.

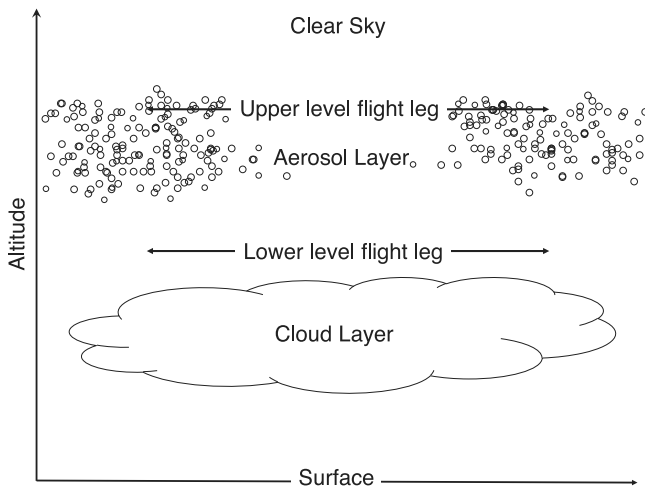


**Figure 1.** J-31 flight leg schematic. The upwelling irradiance along below-aerosol flight legs is influenced only by cloud. Along above-aerosol flight legs, the upwelling irradiance is influenced by cloud and aerosol.

ative properties requires that the retrievals of cloud optical thickness and droplet size are not biased by the presence of aerosol. Haywood *et al.* [2004] describe an apparent indirect aerosol effect in cloud retrievals. Absorbing aerosols overlying clouds reduce the upwelling reflected shortwave radiation from cloud top. Since cloud retrievals generally neglect aerosol above the cloud, the potential exists for a bias that would be indistinguishable from an indirect aerosol effect. Haywood *et al.* [2004] demonstrated that such low biases are theoretically possible in Moderate Resolution Imaging Spectroradiometer (MODIS) [King *et al.*, 1997] retrieved effective cloud droplet radii. The presence of an overlying absorbing aerosol layer resulted in a smaller retrieved effective radius (ratio of the third to second moment of the cloud drop size distribution), potentially indistinguishable in the absence of other observations from a true indirect aerosol effect on cloud radiation.

[4] Reliable retrievals of cloud optical properties are important for testing and supporting climate simulations and because of the large uncertainty in cloud feedbacks on climate. The IPCC Working Group I assessment estimated the indirect aerosol effect to be  $-0.3$  to  $-1.8 \text{ W m}^{-2}$  with a low level of scientific understanding [Forster *et al.*, 2007]. The radiative effects calculated by climate models have been shown to be sensitive to droplet size [Slingo, 1990; Kiehl, 1994] since these models parameterize cloud optical thickness using liquid water path and droplet size. Using such a cloud parameterization and the NCAR Community Climate Model (CCM2), Kiehl [1994] found that (for constant liquid water path and 100% cloud cover) increasing effective radius from 5 to  $10 \mu\text{m}$  increased the amount of absorbed solar radiation at the surface by  $63 \text{ W m}^{-2}$  with little change in the absorbed solar radiation within the atmosphere. Chand *et al.* [2009] demonstrated that the top-of-atmosphere direct aerosol radiative effect depends not only on aerosol type but also the percent fraction and albedo of underlying clouds. They showed that the top-of-atmosphere direct aerosol forcing changed from negative to positive as underlying cloud fraction or cloud albedo increased. In

general, cloud retrievals neglect the presence of aerosols because the variability in aerosol microphysical properties, regional loading, and lifetimes make their inclusion difficult, if not completely impractical.

[5] Twomey and Cocks [1989] demonstrated a method to retrieve cloud optical thickness and effective radius from measurements of cloud reflectance in the visible and near-infrared. By avoiding gas absorption bands, this retrieval technique exploits the variation in bulk liquid water absorption across the shortwave spectrum. At visible and very near-infrared wavelengths less than about 1000 nm, liquid water absorption is negligible but increases with wavelength in the near-infrared. In the near-infrared, a near-linear relationship exists between droplet single-scattering albedo and droplet size. At shorter wavelengths reflectance is primarily a function of cloud optical thickness. At longer wavelengths, reflectance also depends on cloud droplet single-scattering albedo and therefore, droplet size. These relationships have been used to retrieve cloud optical thickness and effective radius in a number of studies [e.g., Foot, 1988; Nakajima and King, 1990] and are the basis for the passive optical remote sensing of clouds from satellite instruments such as MODIS.

[6] In this study, we present retrievals of cloud optical thickness and effective radius from irradiance measurements from the Solar Spectral Flux Radiometer (SSFR) [Pilewskie *et al.*, 2003]. During the Intercontinental Chemical Transport Experiment/Intercontinental Transport and Chemical Transformation of anthropogenic pollution study (INTEX-A/ITCT, hereafter called INTEX-A) [Singh *et al.*, 2006] based out of Portsmouth, New Hampshire, the SSFR was used to measure downwelling and upwelling irradiance from the Sky Research Jetstream-31 (J-31) aircraft. The 14-channel Ames Airborne Tracking Sun photometer (AATS-14) [Russell *et al.*, 1999] measured spectral aerosol optical thickness aboard the J-31 over a similar wavelength range as the SSFR.

[7] We present results from two flights (on 15 and 20 July 2004) when the J-31 flew a low level leg above cloud and below an aerosol layer and then flew an upper level leg above both cloud and aerosol layers (see Figure 1). Thus, the upwelling irradiance measured on the upper legs was influenced by the properties of cloud and aerosol particles in a manner similar to what would be seen from satellite. The below-aerosol leg, however, provided the benefit of characterizing the extinction of the aerosol layer and accounting for its impact on the measured cloud albedo. This unique capability from aircraft provides an opportunity to test the effects of aerosol particles on cloud retrievals. This effect needs to be understood to determine if a systematic bias exists in the cloud retrieval and to distinguish such a bias from a true indirect aerosol effect. Satellite observations are the most critical element in achieving the global and long-term coverage required for quantifying aerosol and cloud forcing of the climate system. However, intensive observations attainable from aircraft studies such as those presented here are necessary to provide validation and closure for the satellite studies.

[8] Cloud retrievals from satellite instruments such as MODIS typically assume that there are no aerosols in the scene because they cannot be unambiguously detected or characterized. Therefore, we show comparisons of SSFR

retrievals of cloud optical thickness and effective radii along the below-aerosol flight leg, which are unaffected by aerosols in the upwelling signal, to those observed by Terra MODIS in near-coincident overpasses. In addition, a sensitivity analysis of SSFR cloud retrievals to aerosols is conducted by including nonabsorbing and absorbing aerosols in forward modeling.

[9] This paper describes the field campaign, central instruments and measurements used in this study (section 2). Sections 3 and 4 describe the forward modeling and cloud retrieval method applied to measured spectral albedo (the ratio of upwelling to downwelling irradiance). The results in section 5 are presented in three parts. Comparisons of SSFR and MODIS cloud retrievals are presented in section 5.1 and comparisons of SSFR cloud retrievals along below- and above-aerosol flight legs are presented in section 5.2. Results from a sensitivity analysis of SSFR retrievals to aerosols are described in section 5.3. A summary and discussion are provided in section 6.

## 2. Background Information

### 2.1. Field Campaign

[10] During July and August 2004, the SSFR was integrated on two aircraft in different field campaigns collaborating under the umbrella of the International Consortium for Atmospheric Research on Transport and Transformation (ICARTT) [Fehsenfeld *et al.*, 2006]. In INTEX-A, the SSFR and AATS-14 were integrated on the J-31 to measure the radiative effects of clouds and aerosols. In the New England Air Quality Study and Intercontinental Transport and Chemical Transformation study (NEAQS-ITCT) [Fehsenfeld *et al.*, 2006], the SSFR was integrated on the NOAA WP-3D aircraft to measure the radiative properties of anthropogenic aerosols over the Northeastern United States.

[11] The combination of measured spectral irradiance and aerosol optical thickness measurements from the J-31, which flew over the Gulf of Maine, made the analysis presented in this paper possible. Since aerosol optical thickness measurements were not available on the WP-3D, only data from the J-31 are presented. Ancillary data came from the ship *Ronald H. Brown*, ground sites in Nova Scotia, Canada, and the NASA DC-8 aircraft.

[12] A regional view of typical aerosol single-scattering albedos (the ratio of aerosol scattering to extinction) was used to guide forward modeling. Aerosol single-scattering albedo from Particle Soot Absorption Photometer and nephelometer measurements was available from NOAA ground monitoring sites at Chebogue Point, NS and Sable Island, NS, Canada, and measurements aboard the *Ronald H. Brown* [Delene and Ogren, 2002; Bates *et al.*, 2006]. However, Angevine *et al.* [2004] suggested that ground level aerosols tend to be separated from the continental flow lofted over the Atlantic Ocean by a cold stable marine boundary layer. In situ aerosol measurements taken aboard the DC-8 during INTEX-A supported this conclusion since aerosols measured above the boundary layer were found to be more absorbing than those at lower altitudes [Bates *et al.*, 2006]. Estimated broadband (350 to 700 nm) aerosol single-scattering albedo from Redemann *et al.* [2006] at J-31 flight altitudes spanned a range of 0.8–0.99. Therefore, in our

forward modeling, we tested the two single-scattering albedo extremes, 0.8 and 1.0, that spanned the range of observed and estimated values.

### 2.2. Measurements

#### 2.2.1. SSFR: Spectral Irradiance and Albedo

[13] The SSFR is a moderate resolution (8–12 nm) spectrometer that spans the wavelength range 350 to 1700 nm. It was calibrated precampaign and postcampaign against a NIST-traceable 1000 W lamp. During the campaign, the instruments were calibrated using a 200 W LiCor lamp to monitor the stability over the duration of the field campaign. In postprocessing a lab-measured cosine correction was applied. To account for variable aircraft attitude, data were filtered to exclude instances when the cosine of solar zenith angle with respect to aircraft deviated more than 5% from that with respect to a horizontal tangent plane.

[14] An additional filter on downwelling irradiance was applied to ensure that conditions above flight level were either cloud-free or that overhead clouds did not contribute to downward scattered irradiance. To accomplish this, we used only SSFR spectra from level flight legs where the measured downward irradiance was within  $\pm 2.5\%$  of modeled clear sky downward irradiance for two wavelengths relatively unaffected by the presence of aerosols (1020 and 1640 nm).

#### 2.2.2. AATS-14: Aerosol Spectral Optical Thickness

[15] The AATS-14 measured aerosol optical thickness at 13 discrete wavelengths over the spectral range 353–2139 nm and columnar water vapor from transmission at 940 nm. Spectral aerosol optical thickness, interpolated to SSFR-RTM wavelengths, was used in forward modeling.

#### 2.2.3. MODIS

[16] MODIS measures radiances [ $\text{W m}^{-2} \text{nm}^{-1} \text{sr}^{-1}$ ] at 36 wavelength bands from the visible to the infrared. In this study, we use the MODIS collection 5 MOD06 Level 2 cloud products [Platnick *et al.*, 2003] at 1 km spatial resolution from Terra that were near-coincident with J-31 flight legs. The MODIS cloud retrievals used in this analysis were cloud optical thickness, droplet effective radius, and liquid water path. Relative uncertainties in the retrieved cloud properties are provided, with the exception of the Band 6 effective radius retrieval as discussed below. A quality assurance file associated with each MODIS granule provided useful information such as retrieval confidence based on the closeness of match between the solution and the limits of the solution space in the forward modeling look up table, cloud type, channel pairs used in the retrieval, and if multiple cloud layers were suspected.

[17] Two specific MODIS data granules used in this study were MOD06\_L2.A2004197.1525.005.2007024002146.hdf from 15 July and MOD06\_L2.A2004202.1540.005.2007024093545.hdf from 20 July. The 20 July granule required special science processing by the MODIS team because the sensing of aerosols in the basic operational algorithm set a flag indicating invalidated cloud retrievals in the J-31 flight region. For 15 July, we use MODIS data of “good” to “very good” retrieval confidence.

[18] Although MODIS Band 7 (2105–2155 nm) is the default wavelength used to provide particle size information in the operational algorithm, another retrieval of cloud particle effective radius uses Band 6 (1628–1652 nm) [King

*et al.*, 1997], which is comparable to the longest wavelength (1625 nm) used in the SSFR cloud retrievals. For non-precipitating water clouds, particles at cloud top tend to be larger than particles below cloud top. Photons in Band 6 have a slightly greater single scattering albedo than those in Band 7. In addition, because forward scattering increases with the dimensionless size parameter,  $x = \frac{2\pi r}{\lambda}$ , ( $r$  is particle radius and  $\lambda$  is wavelength) photons in Band 6 would experience greater forward scattering than those in Band 7. Therefore, compared to Band 7, radiation in Band 6 penetrates deeper into clouds, where droplets are typically smaller than those at cloud top. For this study, we found mean Band 7 MODIS effective radius retrievals were larger than Band 6 retrievals by 0.5 to 1.0  $\mu\text{m}$ . The MODIS Band 6 effective radius does not have a reported uncertainty since it is not aggregated in the operational Level-3 product.

[19] To account for the time difference and subsequent cloud advection (but not evolution) between periods of aircraft and satellite observations, wind profiles from radiosondes launched from the *Ronald H. Brown* were used to calculate an advected J-31 flight track using the technique of *Davis et al.* [2009]. This is required to coordinate sampling volumes from aircraft and satellite platforms in time and space. For the two study cases, satellite overpasses occurred within 10 min of the J-31 flight legs. Since cloud top winds were southwesterly, the advected J-31 flight track locations were southwest of the actual flight legs. It was assumed that the cloud parcel moved uniformly, at the speed and direction of the prevailing wind.

### 3. Forward Modeling

[20] A plane-parallel radiative transfer model (SSFR-RTM) [*Coddington et al.*, 2008; *Bergstrom et al.*, 2003] covering a wavelength range of 300 to 1700 nm, with 1 nm sampling resolution and spectral resolution and filter function equivalent to the SSFR (8–12 nm) is used to simulate the upwelling and downwelling spectral irradiance for a range of cloud optical thickness and droplet effective radii. Molecular absorption for oxygen, ozone, carbon dioxide, water, and methane was calculated using the correlated- $k$  distribution method similar to that described by *Mlawer et al.* [1997]. Molecular scattering optical depth for an atmosphere containing 377 ppm carbon dioxide was calculated by numerical approximation [*Bodhaine et al.*, 1999]. The Discrete Ordinates Radiative Transfer model (DISORT) [*Stamnes et al.*, 1988] was used for the 1-dimensional plane-parallel radiative transfer calculations.

[21] For practical reasons, satellite cloud retrievals are also based on plane-parallel forward calculations. *Marshall et al.* [2006] discussed different 3-dimensional (3D) effects of cloud heterogeneities. Deviations from plane-parallel behavior may lead to biases in optical thickness and effective radius similar in magnitude as those from overlying aerosol layers. Here we focus on the effects of aerosol alone. The 3D cloud effects from stratiform layers are typically less than from, for example, convective clouds, although they may still persist [see, e.g., *Cahalan et al.*, 1994]. Since the footprint of the SSFR in this study is very similar to that of the satellite pixel, heterogeneities are expected to have similar effects on the two different retrievals.

[22] Additional inputs to the model included the top of atmosphere solar irradiance spectrum [*Kurucz*, 1992], surface albedo, day of year, solar zenith angle, atmospheric profiles of temperature, pressure, and humidity, cloud top height, optical thickness, effective radius, and scattering phase function. Aerosols were represented by altitude, optical thickness, single-scattering albedo, and asymmetry parameter. A mean solar zenith angle over short durations (15 min or less) of J-31 flight was used to represent the entire leg with negligible error.

[23] Irradiance spectra from a low-altitude (approximately 100 m), clear-sky flight over the Atlantic Ocean during the campaign were used to obtain a representative sea surface albedo for use in the model. Corrections to account for the transmittance of the atmosphere between the sea surface and the flight level were derived following *Coddington et al.* [2008]. The sea surface was very dark, achieving a maximum albedo of 4% around 400 nm and between 2 and 2.5% elsewhere.

[24] Vertical profiles of pressure, temperature, and water vapor were obtained from meteorological sensors on the J-31. A midlatitude summer standard atmosphere [*Anderson et al.*, 1986] was used to provide oxygen, ozone, carbon dioxide, water vapor, and methane number densities and extend the vertical profile to 37 km.

[25] Mie scattering code [*Evans*, 1998] was used to calculate the scattering properties of cloud drops: extinction (for a liquid water content of 1 g m<sup>-3</sup>), single-scattering albedo, and Legendre series coefficients of the phase function. A gamma distribution typical for water clouds was assumed [*Chylek and Ramaswamy*, 1982]. The Mie calculations were performed for droplet effective radii between 1 and 30  $\mu\text{m}$  in 1  $\mu\text{m}$  increments and over wavelengths from 300 to 2500 nm in 1 nm increments.

[26] Cloud-scattering phase functions were approximated using a 4 stream, 8 discrete ordinate Legendre polynomial expansion. We assumed two values of wavelength-independent aerosol single-scattering albedo, 0.8 and 1.0, as discussed in section 2. A single wavelength-independent aerosol asymmetry parameter of 0.7 was assumed. The aerosol scattering phase function was approximated with the Henyey-Greenstein phase function.

[27] For below-aerosol legs the model-input aerosol optical thickness was equivalent to the measured AATS optical thickness. For above-aerosol legs the aerosol optical thickness of the layer below the J-31 and above the cloud as the difference between the AATS-measured aerosol optical thickness at the two flight levels.

[28] Using these inputs, we calculate the upwelling and downwelling spectral irradiance for clouds of varying optical thickness from 0.5 to 100. Since the irradiance at a single wavelength varies smoothly with optical thickness, we spline-interpolated the irradiance from an initial coarse optical thickness resolution to a resolution of unity. For both dates, six spectral libraries defined by 450 unique pairs of cloud optical thickness and effective radii were created. Three of these libraries were specific to a flight altitude above cloud and below an aerosol layer. The other three were specific to flight legs above cloud and (a large fraction of) aerosol. In each group of three libraries, one corresponded to a baseline case with no aerosol. A second

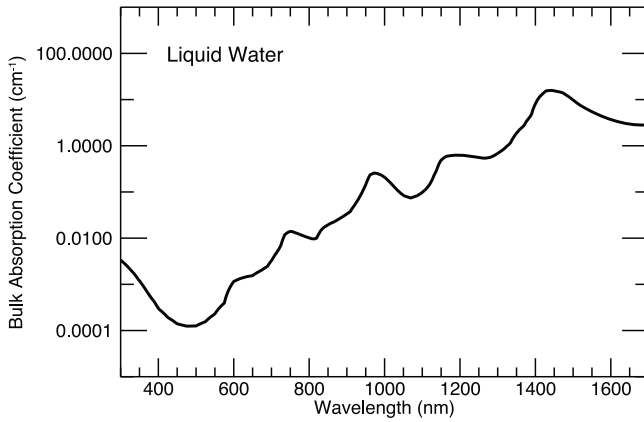


**Figure 2.** Bulk absorption coefficient for liquid water as a function of wavelength.

included nonabsorbing aerosols and the third included absorbing aerosols.

#### 4. Cloud Retrievals

[29] Figure 2 shows the bulk absorption coefficient for liquid water, which is a function of the imaginary part of the complex index of refraction and wavelength. Between 300 and 1700 nm, the bulk absorption coefficient changes by as much as 5 orders of magnitude. Figure 3 shows one minus the single-scattering albedo ( $\omega_o$ ), or co-single-scattering albedo, derived from Mie theory calculations over this same spectral range. Droplet absorption increases with particle size and is negligible at visible wavelengths. Droplet extinction is also dependent upon particle cross section (i.e., volume/size). For fixed liquid water content, scattering varies inversely with particle size since the ratio of droplet surface area to volume decreases as size increases.

[30] Because cloud absorption and extinction (and therefore, cloud optical thickness) depend upon particle size, it is not possible to completely separate the effects of size and optical thickness in the measured cloud reflectance at a single wavelength. However, at visible and very near-

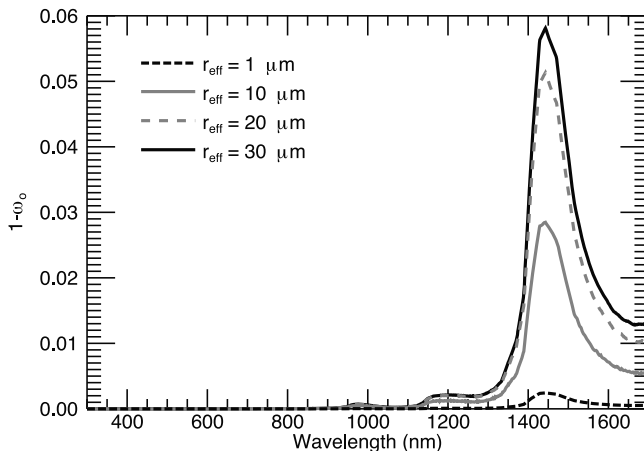


**Figure 3.** Co-single-scattering albedo ( $1 - \omega_o$ ) as a function of wavelength and four different effective radii. Droplet absorption increases with particle size.

infrared wavelengths where absorption is negligible (Figure 3) the magnitude of cloud reflectance will be governed mainly by optical thickness. Conversely, at near-infrared wavelengths, there is a strong dependence on absorption, and therefore particle size. This forms the physical basis for two-wavelength cloud retrievals, illustrated in Figure 4, which shows that in the limit of very thick clouds, curves of optical thickness and effective radius are nearly orthogonal.

[31] A multiwavelength retrieval exploits the same physics exhibited in Figure 4 but with added information. *Twomey and Cocks* [1989] used measurements of cloud reflectance at five wavelengths and a weighted least squares procedure to find the closest match between observations and modeled spectral reflectance. Equation (1) is the chi-square statistic proposed by *Twomey and Cocks* [1989] and adopted by this study using albedo at wavelengths 515, 745, 1015, 1240, and 1625 nm applied in the inversion. Equation (1) consists of two terms, the first of which responds to optical thickness, the second droplet size. Terms  $x_k$  and  $y_k$  denote measured and modeled albedo, respectively, and  $k$  is the index for wavelength.

$$\chi^2 = \frac{1}{60} \sum_{k=1}^5 \left( (5-k)^2 (x_k - y_k)^2 + (k-1)^2 \left( \frac{x_k}{x_1} - \frac{y_k}{y_1} \right)^2 \right) \quad (1)$$

[32] A quantification of the information content in this multispectral retrieval is the topic of a companion paper and will not be discussed here. However, justification for the Twomey-Cocks weighting is the following: at the shortest wavelengths where water does not absorb, the albedo is almost a direct measure of the cloud optical thickness. For this reason, shortest wavelengths are given the greatest weighting for albedo, the first term in equation (1). With increasing absorption from the midvisible through near-infrared, cloud albedo responds to changes in optical thickness and particle size. The response to optical thickness is dampened by normalizing by something nearly equivalent to optical thickness, the albedo at a conservatively scattered

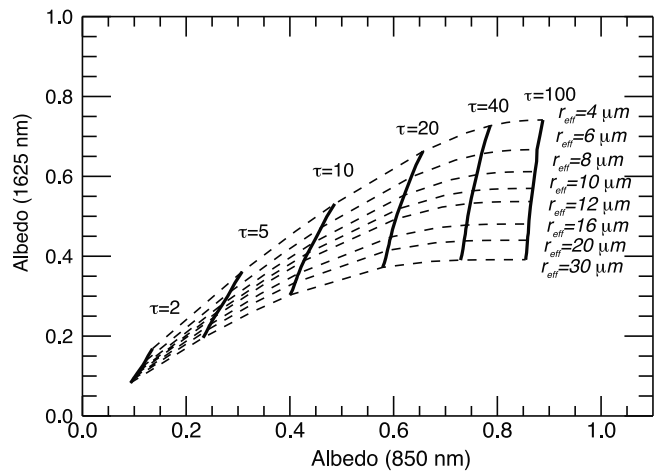


**Figure 4.** Albedo at 850 and 1625 nm. The near-orthogonality between cloud optical thickness and effective radius can be seen at large optical thickness. The solid near-vertical lines represent constant cloud optical thicknesses, and the dashed near-horizontal lines represent constant effective radii.

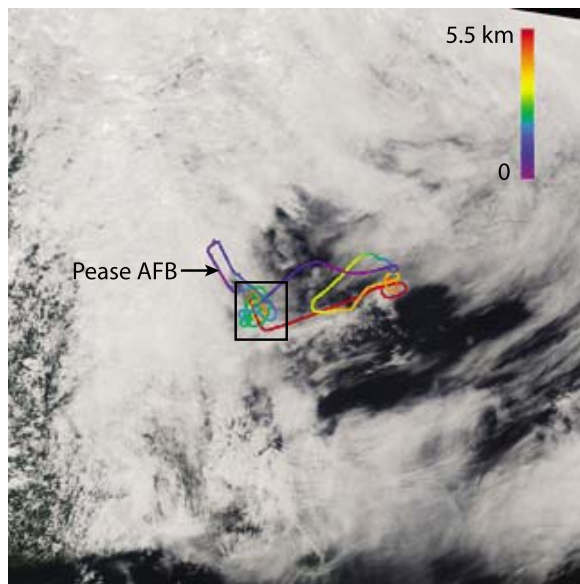


**Figure 5.** MODIS 1 km visible imagery of cloud scene on 15 July with J-31 flight track superimposed. Color coding indicates flight altitude. Data for the below-aerosol case come from section of green flight track near box center; above-aerosol case comes from red flight track.

wavelength ( $k_1 = 515$  nm for our case). Now only the response to droplet size remains so normalized albedos are weighted most strongly at the longest wavelengths, where water is increasingly absorbing, in accordance with Figure 4. The best-fit solution is identified at the minimum residual (i.e., remainder) of equation (1). The minimum residuals obtained in this study are on the order of 3%, which is within the measurement accuracy of the SSFR (3–5%). However, a residual uncertainty is not the same as a retrieval uncertainty which we calculate by propagating a 5% measurement error uncertainty through the chi-square statistic.

[33] In the limit where the cloud drop size is much greater than the wavelength of light (i.e., for size parameters  $\gg 1$ ) and the droplet extinction efficiency ( $Q_{ext}$ ) approaches 2, the liquid water path (LWP) can be calculated from cloud optical thickness ( $\tau$ ) and effective radius ( $r_e$ ):

$$r_e \approx \frac{3}{2} \frac{LWP}{\tau} \quad (2)$$

## 5. Results

[34] For flight legs (see Figure 1) that occurred above cloud and below the aerosol layer spectral albedo was unaffected by the aerosol layer; the downwelling irradiance was influenced by the aerosol layer and molecular scattering and absorption. The above-aerosol flight legs occurred above cloud and most of the aerosol so for these cases the reflected irradiance from cloud top was transmitted through aerosol layers. The downwelling transmitted signal contained relatively small contributions from aerosol. Only 22% of the total layer aerosol (aerosol optical thickness = 0.018 at 499 nm) was above the upper level flight leg on 15 July and 16% (aerosol optical thickness = 0.038 at 499 nm) on 20 July 2004.

[35] This experiment allowed us to fly above and below aerosol layers to monitor albedo changes for two cases: cloud layer only (below aerosol), and cloud plus aerosol layer (above aerosol). SSFR measurements along below-aerosol flight legs can be compared to MODIS retrievals. We do not make comparisons between SSFR and MODIS for above-aerosol scenarios. However, we do compare SSFR retrievals from below- to above-aerosol cases and measure the impact of neglecting the extinction of the aerosol layer on the measured cloud albedo.

[36] The half-power footprint for irradiance is defined as a circle of radius equal to the distance above the scene. Therefore, the SSFR footprint increases with altitude above cloud. Because aircraft-to-cloud distance, and therefore SSFR half-power footprint, were larger for the above-aerosol legs, the upwelling irradiance and retrieved cloud properties are smoother than from the below-aerosol legs due to a larger area contributing to the measurements. A 5% measurement uncertainty was propagated through the cloud retrieval statistic to obtain a relative retrieval uncertainty.

### 5.1. Comparison of SSFR and MODIS Cloud Retrievals (Below-Aerosol Layers)

#### 5.1.1. 15 July

[37] Figure 5 shows MODIS visible imagery of the cloud scene on 15 July with J-31 flight track superimposed. The lower level flight segment (portion of green flight track near box center) of J-31 flight track was approximately 15 min in duration (15.348–15.584 UTC) at 2.4 km altitude in the region 42.9N, 70.6 W. An aerosol layer of optical thickness 0.08 at 499 nm was observed above flight level. The aerosol optical thickness above flight level had no impact on the SSFR cloud retrievals, which were derived using albedo and therefore were independent of changes in incident illumination. 421 SSFR spectra met the filtering criteria described in section 2.2. The flight track was coincident with the MODIS overpass (15.417 UTC). MODIS retrievals from 351 pixels had “good” to “very good” retrieval confidence. The cloud top height and pressure were approximately 1.5 km and 840 hPa, respectively (as determined from MODIS cloud top pressure). The SSFR half-power footprint was approximately 1 km, roughly equal to the 1 km resolution of MODIS.

[38] Figure 6 shows the location of the SSFR and MODIS measurement regions and the cloud retrieval comparisons for effective radius, cloud optical thickness, and cloud liquid water path. A methodology for reconciling the retrieval of physical quantities using measurements from instruments (including SSFR and MODIS) having different sampling characteristics was presented by *Feingold et al.* [2006]. Several factors inherent to the instruments and to the scene contribute to imperfect agreement of retrieved quantities, including but not limited to, sampling volume, spectral resolution and range, accuracy of each instrument, and scene heterogeneity. Some of these are discussed by *Feingold et al.* [2006] and are beyond the scope of the current study.

[39] SSFR retrievals of effective radius tend to be near the lower limit of MODIS retrieved values and in some instances are outside of the uncertainty range. Optical thickness and liquid water path agree within the uncertainty ranges for each instrument. In regions of small MODIS cloud optical thickness ( $< 5$ ), the retrieved MODIS effective



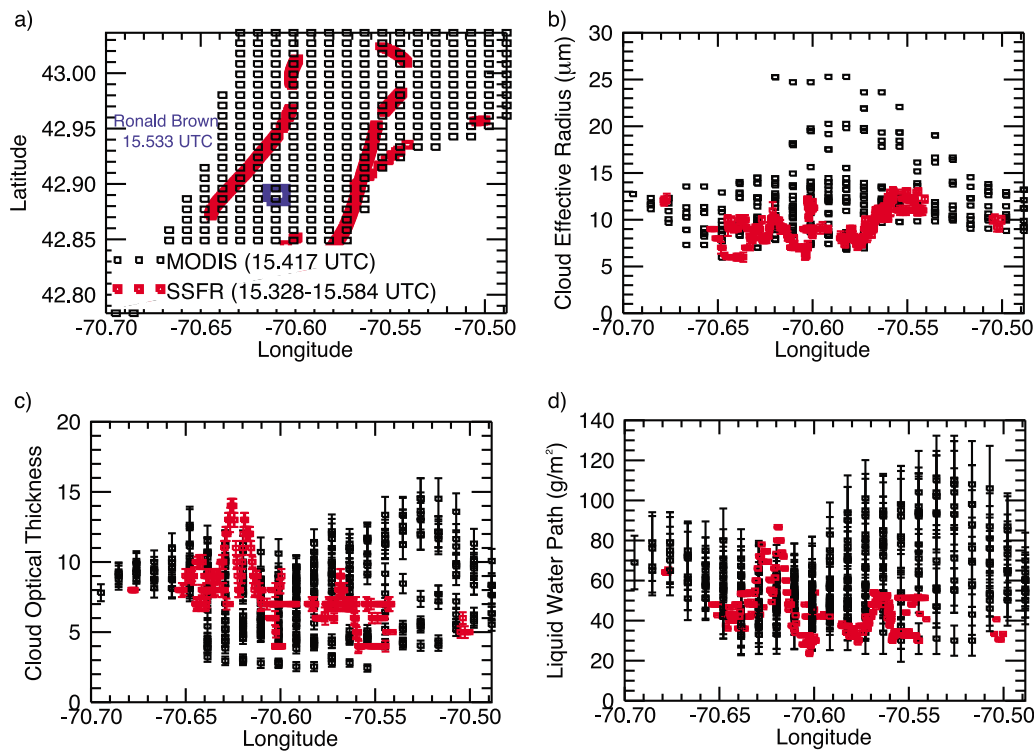


**Figure 6.** (a) Location of SSFR (red) and MODIS (black) for 15 July 2004. Since the J-31 flew a looping pattern through the region, MODIS cloud retrievals are shown from pixels enveloping the flight region. The relative sizes of red and black symbols represent the similarity in spatial coverage between the instruments. *Ronald H. Brown* located at blue square. Retrievals of (b) cloud effective radius, (c) cloud optical thickness, and (d) liquid water path. Red error bars represent the SSFR retrieval uncertainty; black error bars represent the MODIS uncertainty (with the exception of effective radius).

radius is larger (on the order of  $10 \mu\text{m}$ ) than that of the SSFR. For all three variables, a wider distribution was found for MODIS retrievals than for SSFR. This suggests that the larger region encompassed by MODIS pixels may have included greater scene heterogeneity. However, the variance in SSFR retrievals at several longitudes (70.55W, 70.6W, and 70.65W) spanning the latitude range encompassed by MODIS was far less.

### 5.1.2. 20 July

[40] Figure 7 shows MODIS visible imagery of the cloud scene on 20 July. The below-aerosol flight segment (blue section near box center) was approximately 6 min in duration (15.774–15.878 UTC) at 0.8 km altitude in the region 43.1 N, 69.8 W. An aerosol layer of optical thickness 0.23 at 499 nm, approximately three times thicker than that encountered during the 15 July case, was measured above the plane. 365 spectra were found to be suitable for cloud retrievals. A MODIS overpass occurred 6 min earlier, at 15.667 UTC. Due to the low flight altitude above cloud top, the SSFR half-power footprint was smaller than the MODIS pixel.

[41] The wind speed and direction at cloud top (1 km altitude, from a mean MODIS cloud top pressure of 900 hPa) were used to advect the flight track to the time and location of the MODIS overpass. For this date, near-coincident radiosonde data were not available. One launch, nearer to the region of J-31 flight track (see blue box in Figure 8a),

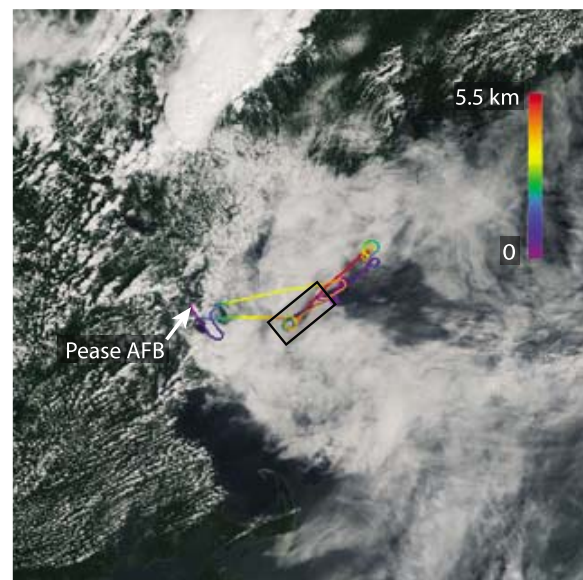


**Figure 7.** Plot details are as in Figure 5 but for 20 July. Data for the below-aerosol case come from section of blue flight track near box center; above-aerosol case comes from orange flight track region.

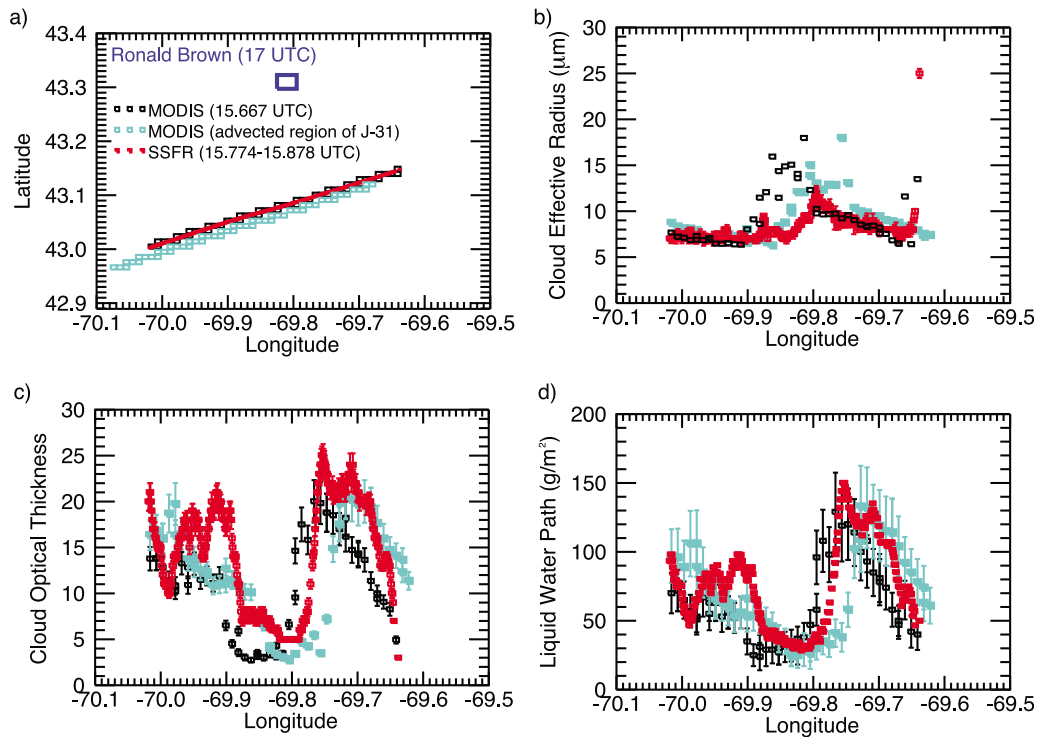


**Figure 8.** (a) Location of SSFR (red) and MODIS measurements in region of nonadvected (black) and advected (light blue) flight regions for 20 July 2004. Advected flight region is approximately 6 km south-west of nonadvected flight region. The difference in spatial resolution is illustrated by the scaled symbol sizes. *Ronald H. Brown* located at blue square. Retrievals of (b) cloud effective radius, (c) cloud optical thickness, and (d) liquid water path are shown. The cloud retrievals corresponding to the light blue MODIS pixels (i.e., from the region of the advected flight track) have been shifted with a constant delta longitude to overlie the same scale as the black MODIS pixel results to ease comparisons. Remaining plot details are as described in Figure 6.

occurred at 17 UTC and measured cloud top wind speeds and direction of  $6.1 \text{ m s}^{-1}$  from  $225^\circ$  at 1 km. Another occurred at 11 UTC at  $43.7^\circ\text{N}$ ,  $68.8^\circ\text{W}$ , approximately 100 km to the southwest, and measured similar winds, indicating that winds remained steady over a long period.

[42] Figure 8 shows the location of the SSFR and MODIS observations and comparisons of retrieved droplet effective radius, cloud optical thickness, and cloud liquid water path. There are large variations of retrieved cloud optical thickness and liquid water path for relatively constant values of effective radius. For both instruments, retrieved cloud optical thickness ranged from approximately 5 to 20, liquid water paths from 20 to  $130 \text{ g m}^{-2}$ , and effective radii from 8 to  $12 \mu\text{m}$ .

[43] In regions of MODIS cloud optical thickness less than 5, the MODIS effective radius exceeded SSFR effective radius by as much as  $10 \mu\text{m}$ . For thicker clouds, MODIS effective radius exceeded SSFR values by  $1\text{--}2 \mu\text{m}$ . Large along-track variability in cloud optical thickness and liquid water path made point-to-point comparisons difficult between SSFR and MODIS. The MODIS pixels in the region of the advected flight track showed improved agreement in the variation in effective radius, cloud optical thickness and liquid water path (especially for longitudes between  $-69.9$  to  $-69.8$  and  $-69.75$  to  $-69.65$ ), justifying the flight-track advection method. Differences at these longitudes approached 2 in cloud optical thickness and were

within the uncertainty range of each instrument for liquid water path. Outside of these longitudes, differences in cloud optical thickness and liquid water path reached values of 10 and  $50 \text{ g m}^{-2}$ , respectively.

## 5.2. Comparison of SSFR Cloud Retrievals (Below- and Above-Aerosol Layers)

### 5.2.1. 15 July

[44] The above-aerosol flight leg (see red flight track segment in Figure 5) was at 5.5 km altitude and in fairly close proximity ( $42.8^\circ\text{N}$ ,  $70.5^\circ\text{W}$ ) to the below-aerosol flight region discussed in section 5.1. It was approximately 3.5 min long (16.003–16.060 UTC) and occurred 35 min after the below-aerosol flight leg. Only 22% of the total aerosol layer was above the J-31 flight level. 103 SSFR spectra were suitable for cloud retrievals.

[45] Figure 9a shows the SSFR measurement region from the below-aerosol (red symbols) and above-aerosol (black symbols) flight legs. The wind speed and direction at cloud top ( $8.3 \text{ m s}^{-1}$  at  $214^\circ$ ) was used to calculate an advected J-31 flight track region (grey), approximately 20 km south-west of the below-aerosol flight leg. Figures 9b–9d compare retrievals of effective radius, cloud optical thickness, and cloud liquid water path from the two legs. Retrievals from the above-aerosol leg were within the same range of those from the below-aerosol leg.



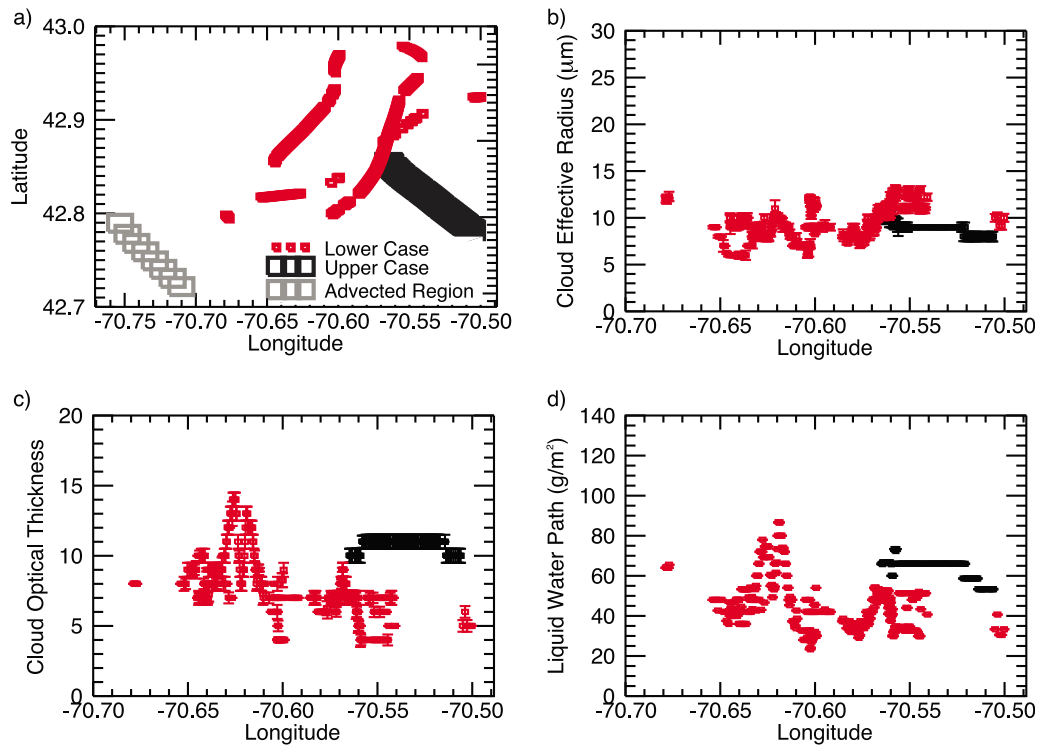


**Figure 9.** (a) Location of SSFR on below-aerosol (red) and above-aerosol (black) flight legs for non-advected (black) flight regions from 15 July 2004. The SSFR half-power footprint is larger on the upper leg relative to the lower leg (represented by scaled sizes of the symbols). Advected flight region (grey) is approximately 20 km southwest of below-aerosol flight region. Retrievals of (b) cloud effective radius, (c) cloud optical thickness, and (d) liquid water path are also shown. Error bars represent a 5% measurement uncertainty propagated through the retrieval.

[46] In the region furthest southwest during the below-aerosol flight leg, clouds had optical thicknesses less than 10 and effective radii less than  $10 \mu\text{m}$ . Cloud optical thickness along the above-aerosol flight leg was greater than 10. Since the aerosol optical thickness contributing to the reflected irradiance from cloud top along the above-aerosol leg was less than 0.1, this suggests that either different clouds were sampled or that clouds evolved during the time between below- and above-aerosol flight legs.

#### 5.2.2. 20 July

[47] The above-aerosol flight leg (orange flight section in Figure 7) was approximately 10 min long (16.030–16.205 UTC) at an altitude of 4.4 km in the region of 43.1N, 69.7 W. It occurred 7.5 min after the below-aerosol leg and in close proximity to it (discussed in section 5.1). 16% of the total above-cloud aerosol layer was above the flight altitude. 205 spectra were used in retrievals along this leg.

[48] Figure 10a shows the location for the below-aerosol (red) and above-aerosol (black) flight legs. The advected flight track region for this leg (not shown) was in very close proximity to the nonadvected flight region. This flight leg was approximately 3–4 km above cloud top, resulting in an SSFR half-power footprint approximately 3–4 times the size of the half-power footprint on the below-aerosol leg.

[49] Figures 10b–10d show SSFR cloud retrievals of effective radius, cloud optical thickness, and cloud liquid water path for both flight legs. Retrieved values of effective radius along both flight legs compare within the uncertainty

range of the SSFR. Retrieved cloud optical thickness and liquid water path along the above-aerosol flight leg showed greater variability than those along the below-aerosol leg. This may have been due to greater scene inhomogeneity in the larger footprint of the above-aerosol flight leg.

#### 5.3. Sensitivity of SSFR Cloud Retrievals to Aerosols

[50] Aerosols were neglected in the SSFR and MODIS cloud retrievals shown in sections 5.1 and 5.2. In this section we show the possible impacts of this omission by comparing to SSFR retrievals from forward modeling with aerosols included.

[51] The affect of aerosols on cloud retrievals can be seen in Figure 4 and is illustrated by *Haywood et al.* [2004]. Figure 4 shows cloud albedos at 850 and 1625 nm. The near-orthogonality between cloud optical thickness and effective radius can be seen at larger optical thickness. For clouds with optical thickness below approximately 40, the behavior deviates from orthogonality. At zero optical thickness, the albedo is equivalent to the surface albedo. An absorbing aerosol layer above cloud top can reduce the albedo, which can affect retrieved cloud optical thickness and effective radius, particularly where cloud optical thickness is less than 40.

[52] Table 1 lists SSFR retrievals of cloud optical thickness ( $\tau_{\text{cloud}}$ ) and effective radius ( $r_e$ ) for 15 and 20 July for flight legs below and above aerosol. Table 1 also shows the

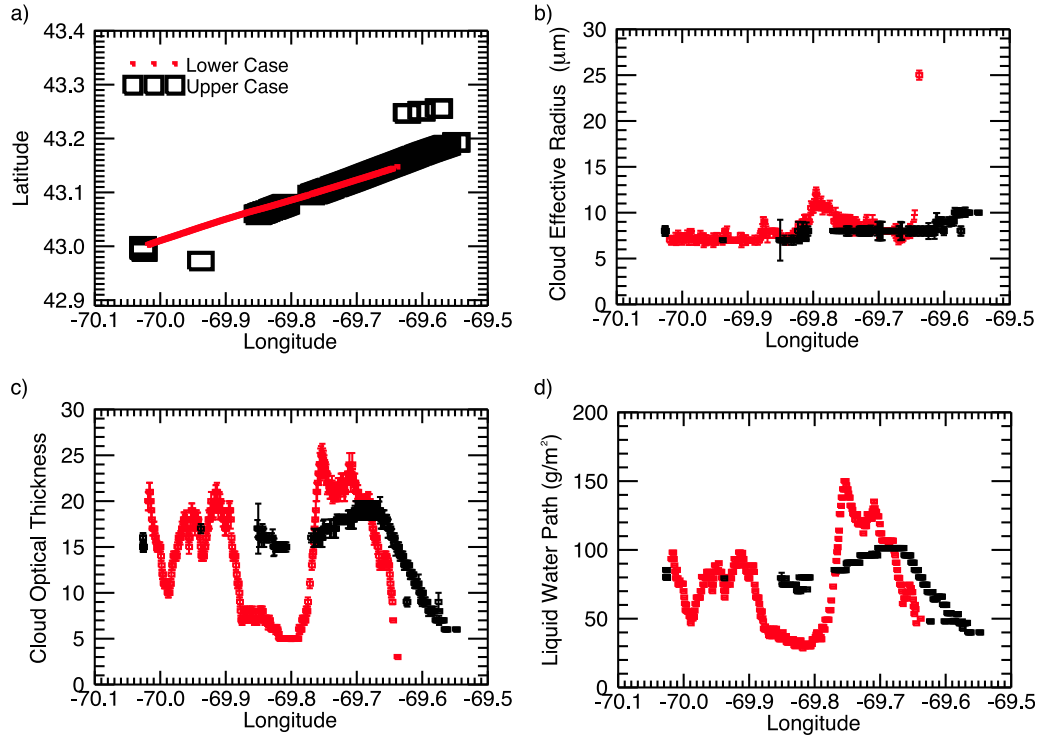


**Figure 10.** (a) Location of below-aerosol (red) and above-aerosol (black) SSFR flight legs for 20 July 2004. The below- and above-aerosol flight legs occurred closely in time, and the advected flight location (not shown) is not significantly different from the above-aerosol flight leg. Retrievals of (b) cloud effective radius, (c) cloud optical thickness, and (d) liquid water path are also shown. Plot details are as described in Figure 9.

mean minimum residual between measured and modeled albedo.

### 5.3.1. Upper Cases: 15 and 20 July

[53] The analysis along the 15 and 20 July upper flight legs suggests that aerosol contributions to the reflected cloud-top irradiance can bias cloud retrievals. Figures 11 and 12 show normalized histograms of the 15 and 20 July retrievals using the libraries described in section 3. These results show that neglecting the aerosol (black) or including

it as nonabsorbing (red) had negligible effect on the mean retrieved cloud properties or their distributions. However, this was not true when assuming that the overlying aerosol layer was absorbing (blue). On 15 July, the mean retrieved cloud optical thickness and effective radius were both larger but within 1 standard deviation of those made when aerosols were neglected. Mean cloud optical thickness increases by approximately 0.5 and mean effective radius by  $1 \mu\text{m}$ . This implies that *neglecting* the overlying absorbing aerosols in

**Table 1.** Mean and Standard Deviations for SSFR Cloud Retrievals of Cloud Optical Thickness and Effective Radius and the Best-Fit for the Below- and Above-Aerosol Flight Regions Defined by the Minimum Residual Between Measured and Modeled Albedo Using the Statistic Defined in Equation (1)<sup>a</sup>

Date	Library	$\tau_{\text{cld}}$	$r_e$ ( $\mu\text{m}$ )	Residual <sup>b</sup> (%)
15 July (below-aerosol case)	Baseline	$7.2 \pm 2.2$	$9.7 \pm 1.7$	$1.1 \pm 0.3$
	+ Nonabsorbing	$7.1 \pm 2.2$	$9.7 \pm 1.8$	$1.0 \pm 0.3$
	+ Absorbing	$7.2 \pm 2.2$	$9.9 \pm 1.9$	$1.0 \pm 0.3$
15 July (above-aerosol case)	Baseline	$10.7 \pm 0.6$	$8.9 \pm 0.6$	$1.1 \pm 0.1$
	+ Nonabsorbing	$10.7 \pm 0.6$	$8.7 \pm 0.5$	$1.2 \pm 0.1$
	+ Absorbing	$11.5 \pm 0.7$	$10.2 \pm 0.8$	$0.8 \pm 0.1$
20 July (below-aerosol case)	Baseline	$14.2 \pm 6.0$	$8.1 \pm 1.4$	$1.2 \pm 0.3$
	+ Nonabsorbing	$13.6 \pm 5.8$	$7.4 \pm 0.8$	$1.0 \pm 0.2$
	+ Absorbing	$13.9 \pm 5.9$	$7.8 \pm 1.1$	$1.0 \pm 0.2$
20 July (above-aerosol case)	Baseline	$14.8 \pm 3.9$	$8.2 \pm 0.7$	$1.0 \pm 0.2$
	+ Nonabsorbing	$14.3 \pm 3.9$	$7.7 \pm 0.4$	$1.3 \pm 0.1$
	+ Absorbing	$18.7 \pm 5.5$	$11.7 \pm 1.4$	$2.4 \pm 0.1$

<sup>a</sup>Results are shown for baseline (cloud only) forward modeling, and for two cases of aerosol; nonabsorbing (aerosol single-scattering albedo = 1), and absorbing (aerosol single-scattering albedo = 0.8). Abbreviations:  $\tau_{\text{cld}}$ , cloud optical thickness;  $r_e$ , effective radius.

<sup>b</sup>Remainder.

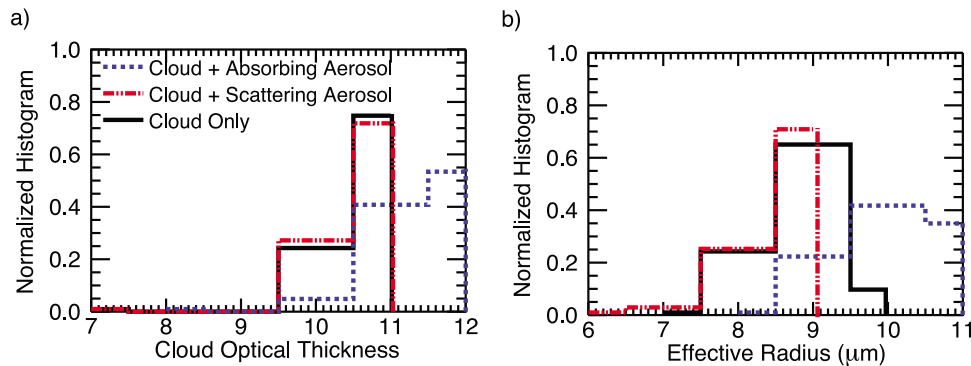


**Figure 11.** Normalized histograms of SSFR (a) cloud optical thickness and (b) effective radius for the various radiative look up tables on 15 July 2004. Baseline results are shown in black. Blue represents results from forward modeling that included the addition of absorbing aerosols above the cloud; red represents results from nonabsorbing aerosols. Results show that neglecting absorbing aerosol above cloud would bias the cloud retrieval to smaller cloud optical thickness and effective radius.

forward modeling calculations biases the cloud retrievals to smaller cloud optical thickness and effective radius. There was a slight increase in the standard deviations of both retrieved distributions when absorbing aerosols were included (on the order of  $\pm 0.1$  to  $0.2$ ).

[54] The sensitivity to absorbing aerosols was greater for conditions on 20 July. *Neglecting* absorbing aerosols resulted in a best fit between measured and modeled irradiances for a cloud of lower optical thickness (by 4) and smaller particle size (by  $3 \mu\text{m}$ ). This again shows that an overlying absorbing aerosol layer reduced the magnitude of the upward irradiance measured above cloud top enough to bias the retrieval toward lower optical thickness and smaller particle size. It also suggests that absorbing aerosols of larger optical thickness, which occurred on 20 July, would reduce upward irradiance measured above cloud top. Subsequently, amplification of the retrieval bias toward even lower optical thickness and smaller particle size would occur.

### 5.3.2. Lower Cases: 15 and 20 July

[55] Retrievals for 15 July along the lower level flight leg showed no change in the mean or distribution of retrieved cloud properties with or without modeled aerosols. This is to be expected since the SSFR retrievals were done using albedo which responds to changes in incident radiation.

Along this flight leg, cloud optical thickness was approximately 7 and effective radius  $9.7 \mu\text{m}$ . Along-track variability (at the 1-standard-deviation level) was  $\pm 2.2$  in cloud optical thickness and slightly less than  $\pm 2 \mu\text{m}$  in effective radius. The along-track variability in SSFR effective radius and cloud optical thickness (red symbols) can also be seen in Figures 6b and 6c from retrieval results where aerosols were neglected in the forward modeling.

[56] For 20 July, the amount of aerosol above flight level was approximately 3 times greater than that measured during 15 July. Reductions in cloud optical thickness and effective radius calculated with the cloud plus nonabsorbing or cloud plus absorbing aerosol library are less than 0.5 in optical thickness and  $1 \mu\text{m}$  in effective radius, respectively. The standard deviation in the minimum residual of the cloud retrievals changed little when aerosols were included in the forward modeling (the along-track variability can also be seen in Figures 8b and 8c).

## 6. Conclusions

[57] For two different dates during INTEx-A, we retrieved effective radius, cloud optical thickness and liquid water path using SSFR albedo measurements made above cloud and below an aerosol layer and then above both the

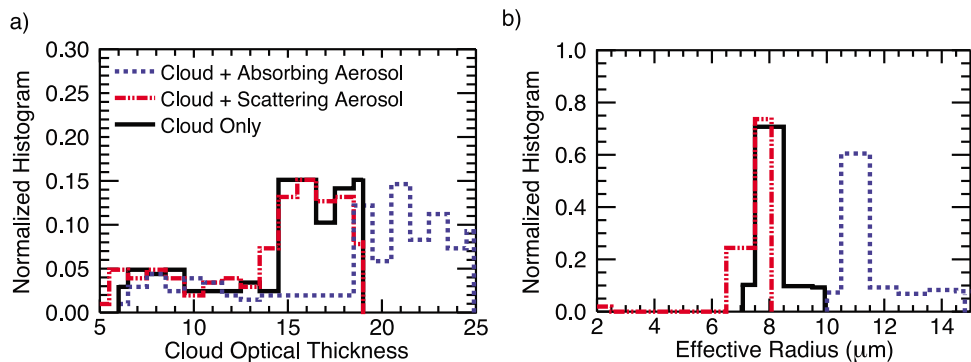


**Figure 12.** Normalized histograms of SSFR (a) cloud optical thickness and (b) effective radius for the various radiative look up tables on 20 July 2004. Plot details are as described in Figure 11.

cloud and aerosol layer. The clouds were nonprecipitating marine stratus off the northeast coast of the United States. These SSFR measurements were spatially collocated with MODIS overpasses and we show comparisons of retrieved cloud properties between the two instruments. The time elapsed between SSFR measurements along the lower level flight legs and MODIS overpasses ranged from 0 to 6 min.

[58] Retrieved values of effective radius from SSFR tended to be smaller than MODIS values and at the low end of MODIS uncertainty estimates. This effect is most pronounced in regions of optical thickness less than 5. Apart from aerosol impacts, differences in surface albedo used in the MODIS and SSFR forward modeling were a potential source for the discrepancy in effective radius. In regions of low cloud optical thickness, the measured upwelling radiation above cloud top will contain a contribution from the surface. The sea surface albedo measured by SSFR was very dark, reaching a maximum of 4% around 400 nm and 2–2.5% elsewhere. The MODIS algorithm (MOD06) [Platnick *et al.*, 2003] assumed a constant diffuse ocean albedo of 5% for all solar bands used in the retrieval. Therefore, the modeled upwelling signal above cloud top (for low optical thickness) would exceed measured. Consequently, a best fit between measured and modeled radiance would occur for a cloud of larger droplet size.

[59] In regions with small variability in cloud properties, retrieved optical thickness between the instruments agreed within their respective uncertainties with the exception of a small number of outliers that differed by up to 2–3. In these same regions, SSFR and MODIS values of liquid water path agreed within the uncertainty range for each instrument. In regions of large variability in cloud properties, differences in cloud optical thickness and liquid water path were as much as 10 and 50 g m<sup>-2</sup>, respectively. For the cases examined, cloud optical thickness ranged from 5 to 25, effective radius from 6 to 25 μm, and liquid water path from 20 to 190 g m<sup>-2</sup>.

[60] By including aerosols in forward modeling, and adopting plausible ranges for aerosol single-scattering albedo and asymmetry parameter, we tested the sensitivity of retrieved (cloud optical thickness, effective radius) pairs to overlying aerosol layers. An irradiance library without aerosols was used to compare cloud retrievals from the libraries that included cloud plus aerosol.

[61] Our study illustrates that an absorbing aerosol layer overlying the cloud reduces the measured upward irradiance. If these absorbing aerosols were not included in forward modeling, a best fit with an optically thinner cloud of smaller droplet effective radii would occur. We found such a potential sensitivity for two cases of overlying aerosol layers with optical thickness 0.06 and 0.19 at 499 nm, and found that the retrieval bias increased with aerosol optical thickness. A significant potential bias was not seen when the modeled overlying aerosol was nonabsorbing. These results support those of Haywood *et al.* [2004] who found that an aerosol layer overlying cloud biased the retrieved cloud droplet effective radius toward smaller values.

[62] The thickness of the aerosol layer overlying cloud determines the degree to which aerosols affect cloud retrievals. Cloud retrievals made using an irradiance library that included overlying absorbing aerosols with optical thickness of 0.06 differ by less than 1 standard deviation from those made with an irradiance library that neglect this

aerosol. However, when retrievals are made with an irradiance library that included absorbing aerosols of a larger optical thickness equal to 0.19, the differences in retrieved cloud properties exceeded 1 standard deviation from those made with an irradiance library that neglected aerosol. This change in effective radius is large enough to cause significant changes in cloud radiative forcing [Slingo, 1990] and emphasizes the need for reliable cloud droplet effective radius retrievals.

[63] These results are significant, especially when noting that these aerosol layers are relatively optically thin, which suggests that the aerosol impact upon cloud retrievals should be understood even under background aerosol conditions. The range in aerosol single-scattering albedo from 0.8 (absorbing) to 1.0 (nonabsorbing) modeled in our forward calculations represents a broad range of possible measured aerosol absorption. If the overlying aerosol layers for our cases had midvisible single-scattering albedos typical of regional, in situ measured ground level aerosol (aerosol single-scattering albedo = 0.96) [Bates *et al.*, 2006], the typical magnitude of their effect on cloud retrievals would lie somewhere between the range of possibilities shown in Table 1.

[64] We show the importance of accounting for aerosols overlying cloud when retrieving cloud optical properties. To get our results, numerous forward modeling calculations were made to investigate the impact of ranges in aerosol optical thickness and single-scattering albedo on the cloud properties. However, since aerosols have variable microphysical properties, loading, and lifetimes, forward modeling under all possible combinations is impractical. We propose a method (T. Vukicevic *et al.*, Characterizing the retrieval of cloud properties from optical remote sensing, submitted to *Journal of Geophysical Research*, 2009) where the aerosol effects on cloud retrievals can be quantified by treating aerosols as a model uncertainty in the existing libraries. Assuming prior knowledge of the aerosol optical thickness and absorption properties overlying the cloud, the outcome of this proposed method is a change in the probability density function of the retrieval over the full range of the optical thickness and effective radius that results from the added uncertainty. The change in the probability density function quantifies systematic and random errors in the retrieval due to the effects of aerosols.

[65] **Acknowledgments.** Numerous people contributed to the ICARTT and INTEx-A field programs. In addition to the work provided by the people referenced in this manuscript, we would like to thank Dan Wolfe for leading the radiosonde effort aboard the *Ronald H. Brown*. We would also like to thank two anonymous reviewers for their comments and suggestions to improve the manuscript. This study was supported by NASA grant NNX08AI83G and NOAA grant NA06OAR4310085.

## References

- Anderson, G. P., S. A. Clough, F. X. Kneizys, J. H. Chetwynd, and E. P. Shettel (1986), AFGL atmospheric constituent profiles (0–120 km), *Tech. Rep. AFGL-TR-86-0110*, Hanscom AFB, Mass.
- Angevine, W. M., C. J. Senff, A. B. White, E. J. Williams, J. Koerner, S. T. K. Miller, R. Talbot, P. E. Johnston, S. A. McKeen, and T. Downs (2004), Coastal boundary layer influence on pollutant transport in New England, *J. Appl. Meteorol.*, **43**, 1425–1437.
- Bates, T. S., *et al.* (2006), Aerosol direct radiative effects over the north-west Atlantic, northwest Pacific, and North Indian Oceans: Estimates

- based on in-situ chemical and optical measurements and chemical transport modeling, *Atmos. Chem. Phys.*, **6**, 1657–1732.
- Bergstrom, R. W., P. Pilewskie, B. Schmid, and P. B. Russell (2003), Estimates of the spectral aerosol single scattering albedo and aerosol radiative effects during SAFARI 2000, *J. Geophys. Res.*, **108**(D13), 8474, doi:10.1029/2002JD002435.
- Bodhaine, B. A., N. B. Wood, E. G. Dutton, and J. R. Slusser (1999), On Rayleigh optical depth calculations, *J. Atmos. Ocean. Tech.*, **16**, 1854–1861.
- Cahalan, R. F., W. Ridgway, W. J. Wiscombe, and T. L. Bell (1994), The albedo of fractal stratocumulus clouds, *J. Atmos. Sci.*, **51**(16), 2434–2455.
- Chand, D., R. Wood, T. L. Anderson, S. K. Satheesh, and R. J. Charlson (2009), Satellite-derived direct radiative effect of aerosols dependent on cloud cover, *Nat. Geosci.*, **2**, 181–184.
- Chylek, P., and V. Ramaswamy (1982), Simple approximation for infrared emissivity of water clouds, *J. Atmos. Sci.*, **39**, 171–177.
- Coakley, A. J., and C. D. Walsh (2002), Limits to the aerosol indirect radiative effect derived from observations of ship tracks, *J. Atmos. Sci.*, **59**, 668–680.
- Coddington, O. M., K. S. Schmidt, P. Pilewskie, W. J. Gore, R. W. Bergstrom, M. Román, J. Redemann, P. B. Russell, J. Liu, and C. C. Schaaf (2008), Aircraft measurements of spectral surface albedo and its consistency with ground-based and space-borne observations, *J. Geophys. Res.*, **113**, D17209, doi:10.1029/2008JD010089.
- Davis, S. M., L. M. Avallone, B. H. Kahn, K. G. Meyer, and D. Baumgardner (2009), Comparison of airborne in situ measurements and Moderate Resolution Imaging Spectroradiometer (MODIS) retrievals of cirrus cloud optical and microphysical properties during the Midlatitude Cirrus Experiment (MidCiX), *J. Geophys. Res.*, **114**, D02203, doi:10.1029/2008JD010284.
- Delene, D. J., and J. A. Ogren (2002), Variability of aerosol optical properties at four North American surface monitoring sites, *J. Atmos. Sci.*, **59**, 1135–1150.
- Evans, F. K. (1998), The spherical harmonic discrete ordinate method for three-dimensional atmospheric radiative transfer, *J. Atmos. Sci.*, **55**, 429–446.
- Fehsenfeld, F. C., et al. (2006), International Consortium for Atmospheric Research on Transport and Transformation (ICARTT): North America to Europe—Overview of the 2004 summer field study, *J. Geophys. Res.*, **111**, D23S01, doi:10.1029/2006JD007829.
- Feingold, G., R. Furrer, P. Pilewskie, L. Remer, Q. Min, and H. Jonsson (2006), Aerosol indirect effect studies at Southern Great Plains during the May 2003 intensive operations period, *J. Geophys. Res.*, **111**, D05S14, doi:10.1029/2004JD005648.
- Foot, J. S. (1988), Some observations of the optical properties of clouds: Part I. Stratocumulus, *Q. J. R. Meteorol. Soc.*, **114**, 129–144.
- Forster, P., et al. (2007), Changes in atmospheric constituents and in radiative forcing, in *Climate Change 2007: The Physical Science Basis. Contribution of Working Group I to the Fourth Assessment Report of the Intergovernmental Panel on Climate Change*, edited by S. Solomon et al., Cambridge Univ. Press, Cambridge, U. K.
- Haywood, J. M., S. R. Osborne, and S. J. Abel (2004), The effect of overlying absorbing aerosol layers on remote sensing retrievals of cloud effective radius and cloud optical depth, *Q. J. R. Meteorol. Soc.*, **130**, 779–800.
- Kiehl, J. T. (1994), Sensitivity of a GCM climate simulation to differences in continental versus maritime cloud drop size, *J. Geophys. Res.*, **99**, 23,107–23,115.
- King, M. D., S.-C. Tsay, S. E. Platnick, M. Wang, and K. N. Liou (1997), Cloud retrieval algorithms for MODIS: Optical thickness, effective particle radius, and thermodynamic phase, *Tech. Rep. ATBD-MOD-05*, NASA Goddard Space Flight Cent., Greenbelt, Md.
- Kurucz, R. L. (1992), Synthetic infrared spectra, in *Infrared Solar Physics*, edited by D. M. Rabin and J. T. Jeffries, *IAU Symp. 154*, Kluwer Acad., Norwell, Mass.
- Marshak, A., S. Platnick, T. Varnai, G. Wen, and R. F. Cahalan (2006), Impact of three-dimensional radiative effects on satellite retrievals of cloud droplet sizes, *J. Geophys. Res.*, **111**, D09207, doi:10.1029/2005JD006686.
- Mlawer, E. J., S. J. Taubman, P. D. Brown, M. J. Iacono, and S. A. Clough (1997), Radiative transfer for inhomogeneous atmospheres: RRTM, a validated correlated-k model for the longwave, *J. Geophys. Res.*, **102**(D14), 16,630–16,682.
- Nakajima, T., and M. D. King (1990), Determination of the optical thickness and effective particle radius of clouds from reflected solar radiation measurements: I. Theory, *J. Atmos. Sci.*, **47**, 1878–1893.
- Peng, Y., U. Lohmann, R. Leaith, C. Banic, and M. Couture (2002), The cloud albedo-cloud droplet effective radius relationship for clean and polluted clouds from RACE and FIRE.ACE, *J. Geophys. Res.*, **107**(D11), 4106, doi:10.1029/2000JD000281.
- Pilewskie, P., J. Pommier, R. Bergstrom, W. Gore, S. Howard, M. Rabbette, B. Schmid, P. V. Hobbs, and S. C. Tsay (2003), Solar spectral radiative forcing during the Southern African Regional Science Initiative, *J. Geophys. Res.*, **108**(D13), 8486, doi:10.1029/2002JD002411.
- Platnick, S., P. A. Durkee, K. Nielsen, J. P. Taylor, S.-C. Tsay, M. D. King, R. J. Ferek, P. V. Hobbs, and J. W. Rottman (2000), The role of background cloud microphysics in the radiative formation of ship tracks, *J. Atmos. Sci.*, **57**, 2607–2624.
- Platnick, S. E., M. D. King, S. A. Ackerman, W. P. Menzel, B. A. Baum, J. C. Riedi, and R. A. Frey (2003), The MODIS cloud products: Algorithms and examples from Terra, *IEEE Trans. Geosci. Remote Sens.*, **41**(2), 459–473, doi:10.1109/TGRS.2002.808301.
- Redemann, J., P. Pilewskie, P. B. Russell, J. M. Livingston, S. Howard, B. Schmid, J. Pommier, W. Gore, J. Eilers, and M. Wendisch (2006), Airborne measurements of spectral direct aerosol radiative forcing in the Intercontinental Chemical Transport Experiment/Intercontinental Transport and Chemical Transformation of anthropogenic pollution, *J. Geophys. Res.*, **111**, D14210, doi:10.1029/2005JD006812.
- Russell, P. B., J. M. Livingston, P. Hignett, S. Kinne, J. Wong, A. Chien, R. Bergstrom, and P. V. Hobbs (1999), Aerosol-induced radiative flux changes off the United States mid-Atlantic coast: Comparison of values calculated from Sunphotometer and in situ data with those measured by airborne pyranometer, *J. Geophys. Res.*, **104**(D2), 2289–2307.
- Singh, H. B., W. H. Brune, J. H. Crawford, D. J. Jacob, and P. B. Russell (2006), Overview of the summer 2004 Intercontinental Chemical Transport Experiment: North America (INTEX-A), *J. Geophys. Res.*, **111**, D24S01, doi:10.1029/2006JD007905.
- Slingo, A. (1990), Sensitivity of the Earth's radiation budget to changes in low clouds, *Nature*, **343**, 49–51.
- Stamnes, K., S.-C. Tsay, W. Wiscombe, and K. Jayaweera (1988), Numerically stable algorithm for discrete-ordinate-method radiative transfer in multiple scattering and emitting layered media, *Appl. Opt.*, **27**(12), 2502–2509.
- Twomey, S. (1974), Pollution and the planetary albedo, *Atmos. Environ.*, **8**, 1251–1256.
- Twomey, S. (1991), Aerosols, clouds, and radiation, *Atmos. Environ.*, **25A**, 2435–2442.
- Twomey, S., and T. Cocks (1989), Remote sensing of cloud parameters from spectral reflectance in the near-infrared, *Beitr. Phys. Atmos.*, **62**, 172–179.
- Wilcox, E. M., G. Roberts, and V. Ramanathan (2006), Influence of aerosols on the shortwave cloud radiative forcing from North Pacific oceanic clouds: Results from the Cloud Indirect Forcing Experiment (CIFEX), *Geophys. Res. Lett.*, **33**, L21804, doi:10.1029/2006GL027150.

O. M. Coddington and K. S. Schmidt, Laboratory for Atmospheric and Space Physics, University of Colorado, Campus Box 392, Boulder, CO 80309, USA. (odele.coddington@lasp.colorado.edu)

W. J. Gore, NASA Ames Research Center, MS 245-4, Moffett Field, CA 94035-1000, USA.

J. Livingston, SRI International, G-179, 333 Ravenswood Ave., Menlo Park, CA 94025, USA.

P. Pilewskie, Laboratory for Atmospheric and Space Physics, University of Colorado, Campus Box 311, Boulder, CO 80309, USA.

S. Platnick and G. Wind, NASA GSFC, Code 613.2, Greenbelt, MD 20771, USA.

J. Redemann and P. B. Russell, NASA Ames Research Center, MS 245-5, Moffett Field, CA 94035-1000, USA.

T. Vukicevic, NOAA Atlantic Oceanographic and Meteorological Laboratory, 4301 Rickenbacker Causeway, Miami, FL 33149, USA.